Effective Selection and Targeted Passivation for Different Defect Types by Ammonium Salts in Perovskite Solar Cells

*Yifang Qi[a], Jeffrey Aguinaga[b], Tanguy Terlier[c,d], Chuchu Qiu[e], Haixin Zhang[f], Saroj Upreti[b], Italian Johnson[a], Jordan Glover[a], Rui Hang[e], Sheng He[e], Paresh Chandra Ray[a], Kun Wang[f,g], Xiaodan Gu[b], Derek Patton[b], Tianquan Lian[e], Qilin Dai[a]**

[a] Department of Chemistry, Physics, and Atmospheric Sciences, Jackson State University, Jackson, MS, 39217, United States.

[b] School of Polymer Science and Engineering, Center for Optoelectronic Materials and Devices, The University of Southern Mississippi, Hattiesburg, MS, 39406, United States.

[c] SIMS laboratory, Shared Equipment Authority, Rice University, Houston, TX, 77005, United States.

[c] Department of Chemical & Biomolecular Engineering, Rice University, Houston, TX 77005, United States.

[c] Department of Chemistry, Emory University, Atlanta, GA 30322, United States.

[d] Department of Physics, University of Miami, Coral Gables, Florida 33146, United States

[e] Department of Chemistry, University of Miami, Coral Gables, Florida 33146, United States

[*] Corresponding author: Qilin Dai, Email: qilin.dai@jsums.edu

Keywords: perovskite solar cells, targeted passivation, alkyl chain salts, vacancy, DFT calculation

Abstract

The optimal selection of alkyl chains and halogen ions in ammonium salts for addressing specific defect types in perovskite films remains unclear although ammonium salts emerged as a promising strategy to enhance performance of perovskite solar cells (PSCs). Herein, we introduced four ammonium salts with different alkyl chain types and halogen ions to passivate perovskite films.

Branched-alkyl chain ammonium salts exhibited superior passivation effects compared to linear-alkyl chain salts, with the alkyl chain structure having a more significant impact on device performance than the halogen ion component. In addition, DFT calculations were performed to investigate which defect types in perovskite films are most effectively passivated by different alkyl chain types and halogen ions in ammonium salts. Branched-alkyl chain ammonium salts demonstrated superior passivation effects on V_{Pb} and V_{FA} defects in perovskite films compared to linear-alkyl chain salts, while exhibiting similar passivation effects for V_I defects. PSCs passivated with tert-OAI achieved an impressive efficiency of 25.49%, with a V_{oc} of 1.19 V, a J_{sc} of 25.40 mA/cm², and an FF of 84.34%. This work highlights a targeted ammonium salt passivation strategy tailored to address different defect types in perovskite films, accounting for variations in perovskite composition and fabrication environments.

1. Introduction

Photovoltaic devices based on organic-inorganic lead halide perovskite have attracted extensive attention owing to their high carrier mobility, long carrier diffusion lengths, high optical absorption coefficient, and low cost[1]. The power conversion efficiency (PCE) of single perovskite solar cells (PSCs) has reached 26.7%, and they are considered promising next-generation solar cells[2]. However, the record PCE is still lower than the Shockley-Queisser limit efficiency (33.7%)[3], and the stability of PSCs is still far from the commercial application standard. Perovskite films are typically fabricated using solution-based methods at low temperatures, which makes iodide within the perovskite readily volatile. As a result, the perovskite film surface and grain boundary exhibit numerous defects and traps[4,5]. In addition, interface defects between device layers can cause performance losses by hindering charge carrier transport across layers[6,7]. These defects and traps are considered non-radiative recombination centers that limit device performance[8,9]. Adjusting the perovskite precursor solution would control the defect and traps in perovskite bulk. However, most of the defects within perovskite bulk are shallow, and the defects at perovskite surface and grain boundaries (GBs) are deep-level traps, which is critical to the performance of PSCs[1,10]. Furthermore, the light and water would influence the perovskite surface, so the interface passivation between the perovskite and hole transport layer has been demonstrated as a promising method to modify the defects due to no unfavorable influence on the perovskite growth.

Many materials have been used to passivate the perovskite surface, including small organic molecules, polymers, metal cations, halogen ions, etc. The diverse functional groups of these passivation materials can address the wide range of defect types in perovskite films, resulting in high-quality films with fewer non-radiative recombination centers and improved device performance[11]. Zhang *et al.* fabricated PSCs using N-carbamoyl-2-propan-2-ylpent-4-enamide (Apronal) for passivation, which formed a crosslinked polymer (P-Apronal) with the perovskite films. The P-Apronal passivation effectively improve efficiency to 25.09% and suppressed the migration of I^- ions[12]. He *et al.* studied the influence of the aniline derivative N-(4-cyanophenyl)acetamide (CAL) on the passivation of Pb-related defects in perovskite films, and a champion device with PCE of 24.35% was obtained[13]. Liu *et al.* investigated the surface passivator 3-(2-aminoethyl)pyridine (3-PyEA) for PSCs, which effectively modified the V_I and V_{FA} of perovskite films, achieving an efficiency of 25.65%[14]. Although significant progress has

been made in passivating defects in PSCs, the specific types of defects that can be addressed by different materials remain unclear, as does the relationship between defect types and the corresponding organic functional groups used for passivation.

In addition, alkyl-chain ammonium salt is a popular passivation material because the ammonium salt has an affinity for coupling with $[PbX_6]^{4-}$ octahedron[15]. Zheng *et al.* synthesized 1-naphthylmethylammonium formate (NMACOOH) to passivate the perovskite film surface, forming a thermally stable PbI_2-NMACOOH adduct, which increased the efficiency of PSCs to 24.75%[16]. Wu *et al.* introduced 2-amidinopyrimidine hydrochloride (APC) to the surface of perovskite films, which passivated the iodine vacancies and compensated the formamidine vacancies. After APC passivation, the certified efficiency of the devices reached 24.51%, and the devices also exhibited excellent long-term and operational stability[17]. Liu *et al.* compared the passivation effect of 1.6-hexamethylene-diamine dihydriodide ($HDAI_2$), 1,3-propane-diamine dihydriodide ($PDAI_2$), and 1.4-butane-diamine dihydriodide ($BDAI_2$) on the performance of PSCs, and the efficiency of devices with $BDAI_2$ reached 23.1%[18]. Among these alkyl-chain ammonium salts, the n-octylammonium salt demonstrated excellent passivation effects, and it has often been used as a control in studies on perovskite devices with passivation[19–30]. In addition, the counter ion of alkyl-chain ammonium salts are usually used as halogen ions, which could also heal the defects of perovskite films. Liu *et al.* introduced high-electronegativity halogen groups (4-fluorobenzamide and 4-chlorobenzamide) on the surface of perovskite films, and the halogen functional group reduced the defect density and increased carrier lifetime. The efficiency of the champion device reached 21.35%[31]. Pan *et al.* designed four different halogenated capping layers to modify PSCs, and the optimal devices with 4-bromobenzylammonium passivation achieved an efficiency of 21.13%[32].

Although the above materials have demonstrated positive passivation effects on PSCs, they may not be suitable for all perovskite fabrication environments or film compositions. This is because the defect types in perovskite films can vary significantly depending on the fabrication process. Typically, two dominant types of defects are involved in perovskite fabrication: organic cation vacancies and lead vacancies. To make ammonium salt passivation more targeted and effective, it is essential to investigate the detailed passivation mechanisms of perovskite films using ammonium salts with various organic functional groups. Furthermore, it is crucial to identify

which types of alkyl-chain ammonium salts are best suited to address specific defects in perovskite films, such as organic cation or lead vacancies. Understanding the relationship between passivating agents and defect types is critical, as defect types directly impact device performance and are significantly influenced by the composition of the perovskite film and the fabrication environment.

In this work, we utilized four different kinds of ammonium salts to modify the defects and traps in the devices using an interface passivation strategy. The functional groups in two sides (cation and anion) for the ammonium salts could both passivate the surface defects of perovskite films. First, to investigate the passivation effects of the alkyl chain in the cation side of ammonium salts, the linear- and branched-alkyl chain with iodide as anion are used to passivate the PSCs. The halogen functional group in ammonium salts is also optimized to understand the influence of the anion side on the performance of the devices. The passivation effect of ammonium salts is separated into the alkyl chain and halogen ions to understand device performance enhancement further.

Second, the introduction of passivation materials on the perovskite surface also adjusts the bandgap and electric field of the devices through the interaction between perovskite and passivation materials. Based on our device fabrication environment, the composition of perovskite films, and the defects of our devices, we optimized a series of alkyl chains and halogen ions in the ammonium salts.

Third, we utilized DFT calculation to investigate the mechanism of passivation effects on the three different vacancy defect types (V_{FA}, $V_{Pb,}$ and V_I) of perovskite films. The halogen ions are preferred to passivate the V_I of perovskite films, and three passivation conditions (halogen ions on the surface of perovskite, halogen ions completely filling V_I and the halogen ions partly filling V_I) have been studied. Furthermore, we compared the passivation effects of linear- and branched-alkyl chain in ammonium salt perovskite films with V_{Pb} and V_{FA}. Therefore, we provide a targeted passivation strategy for PSCs by ammonium salts with different types of alkyl chains and halogen ions, which could be selected to passivate the perovskite films based on the different perovskite fabrication environments and perovskite compositions.

2. Results and discussions

Figure 1 shows the overview of this work. We utilized n-OAI, tert-OAI, tert-OABr, and tert-OACl to modify the surface of perovskite films. Figure 1a exhibits the structure of passivation materials

with different alkyl-chain and halogen ions in the ammonium salts. The alkyl-chain and halogen ions have different passivation effects on the various defects in the perovskite surface, and the defect types of perovskite films are shown in Figure 1b. We fabricate PSCs with four ammonium salts passivation, and the structure of the devices is shown in Figure 1c. After the targeted passivation by tert-OAI for perovskite films, the efficiency of PSCs presents a 10% improvement from 23.17% to 25.49%.

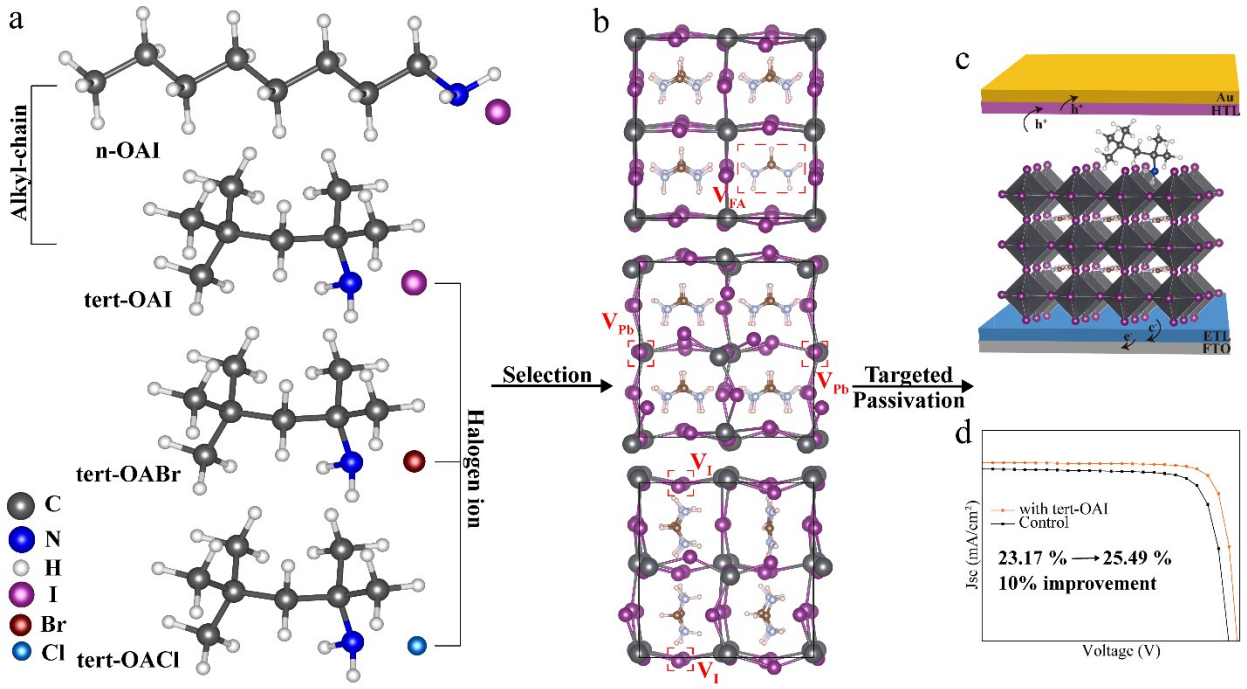

Figure 1 a. The structure of passivation ammonium salts (n-OAI, tert-OAI, tert-OABr and tert-OACl); b. The vacancy defect types (from top to bottom: V_{FA}, V_{Pb} and V_I) of perovskite films; c. The structure of PSCs with passivation; d. The J-V curves of devices with and without tert-OAI passivation.

To investigate the passivation influence of ammonium salts with different ions on the perovskite film crystallinity and quality, we compared the X-ray diffraction (XRD) patterns and GIWAXS of perovskite films with and without passivation, as exhibited in Figure S1 and Figure S2. Furthermore, to understand the interaction between linear-alkyl-chain and branched-alkyl-chain of ammonium salts on the perovskite surface, the XRD patterns of PbI_2 with n-OAI (linear-alkyl-chain) and tert-OAI (branched-alkyl-chain) and the Fourier transform infrared spectroscopy (FTIR)

spectra of perovskite films with and without passivation layers were measured, which are shown in Figure S3.

The top-view scanning electron microscopy (SEM) was carried out to study the morphology and surface topography of pristine perovskite film and the films with different passivation, as illustrated in Figures 2a to 2e. It is seen that the grain size of modified perovskite films is marginally larger than the pristine perovskite films, and the grain size distributions are shown in Figure S4. The grain size significantly increases from ~1227 nm of the pristine film to ~1394 nm of tert-OACl, ~1576 nm of tert-OACl, ~1259 nm of tert-OABr, and ~1233 nm of n-OAI passivated films, which are consistent with the XRD results. In addition, the roughness of perovskite films is characterized by atomic force microscope (AFM) images. The surface roughness of the pristine perovskite film is ~43.5 nm, which decreases to ~35.8 nm of tert-OABr perovskite film, ~35.2 nm of tert-OAI perovskite film, ~33.3 nm of tert-OACl perovskite film, and ~35.4 nm of n-OAI perovskite film, respectively. From the top-view SEM and height AFM images, the smoother and larger grain size of perovskite films is obtained after passivation, which decreases the defect density in the grain boundaries and suppresses the charge recombination[33]. And Figure S5 shows the cross-section of SEM images of perovskite films with different passivations. However, there are no obvious 2D perovskite structures observed, which is attributed to the limited amount of 2D perovskite. In addition, the cross-section of the surface potential of pristine perovskite film and perovskite films passivated by tert-OAI, tert-OACl, tert-OABr, and n-OAI are shown in Figure S6. Compared to the pristine perovskite film, the surface potential values of passivated perovskite films are significantly lower, indicating reduced charge carrier trapping at the perovskite surface and improved charge transport within the devices.[34]. The passivators distribute within 10 nm on top of the perovskite surface which is obtained by Time-of-flight secondary ion mass spectroscopy (ToF-SIMS) and exhibited in Figure S7.

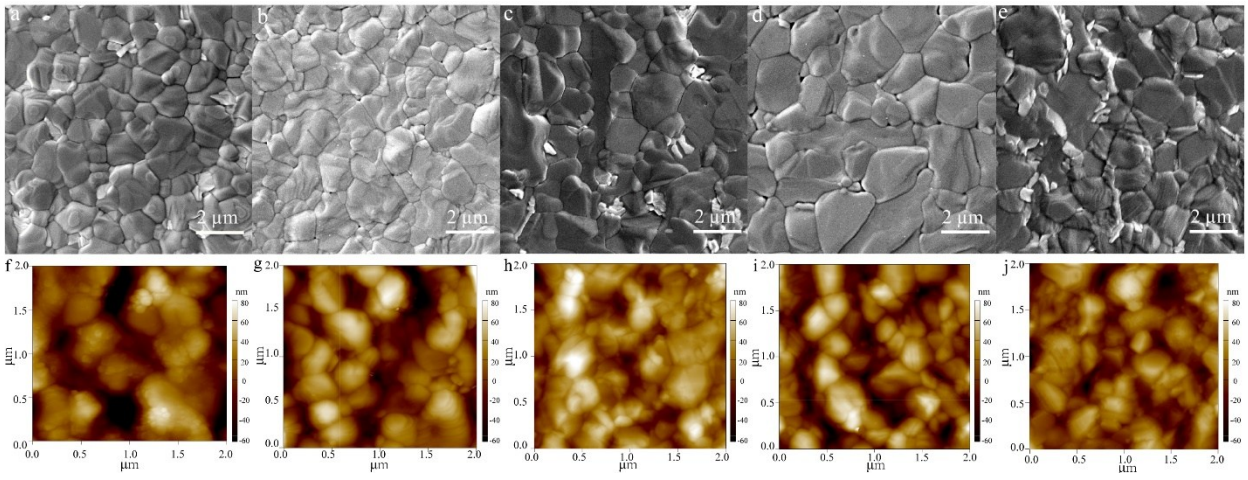

Figure 2 a-e. The top-view SEM images of perovskite without passivation (a), with tert-OABr (b), tert-OACl (c), tert-OAI (d) and n-OAI (e); f-j. The AFM images of perovskite without passivation (f), with tert-OABr (g), tert-OACl (h), tert-OAI (i) and n-OAI (j).

To study the chemical interactions between passivation materials and perovskite films, X-ray photoelectron spectroscopy (XPS) was performed. Figures 3a and 3b present the XPS spectra of the Pb 4f region for a control (unpassivated) perovskite film and films with tert-OAI, n-OAI, tert-OABr, and tert-OACl passivation. The control perovskite film exhibits two peaks at 142.72 eV and 137.85 eV due to spin-orbit coupling assigned to Pb-$4f_{5/2}$ and Pb-$4f_{7/2}$[35]. Figures 3c and 3d exhibit the XPS spectra of the I 3d region for perovskite films with and without surface modification by tert-OAI, n-OAI, tert-OABr, and tert-OACl. The pristine perovskite film shows two peaks at 630.25 eV and 618.77 eV related to the I-$3d_{3/2}$ and I-$3d_{5/2}$[36]. The Pb 4f peaks shift to higher binding energy for the perovskite films after being passivated by tert-OAI, n-OAI, tert-OABr, and tert-OACl, which suggests a decrease of electron density around Pb^{2+} due to the strong electronic interaction between electronegative ammonium and undercoordinated Pb^{2+} [37,38]. These results confirm that the undercoordinated Pb^{2+} could be passivated by ammonium salts, and the charge transportation in the devices is also improved[37]. Furthermore, the shift of I 3d peaks of perovskite films with passivation layers suggests that the binding interaction of Pb and I in the perovskite films has been improved by the ammonium salt passivation layers, and the orbitals of Pb and I are related to the optical band gap of the films with passivation layers. The XPS peaks of Pb 4f and I 3d of the films with passivation layers all shift to higher binding energy, indicating the

Fermi level has been impacted by the ammonium salt layers[39], which has also been observed in other studies about perovskite solar cells[38,40–42]. And the results are also consistent with the KAFM and UPS results.

The XPS spectra of Cl-2p were also obtained and are exhibited in Figure 3e. The perovskite films with tert-OACl modification clearly exhibited a Cl-2p peak not observed in other perovskite films[43]. In Figure 3f, the perovskite with tert-OABr passivation shows the strongest Br-3d peak for the XPS among the perovskite films. The XPS peaks of Cl and Br confirm the passivation materials are on the surface of perovskite films. To understand the influence of passivation materials on the electronic structure of perovskite films, ultraviolet photoelectron spectroscopy (UPS) of perovskite films was performed. The work function is calculated from the secondary electron cutoff energy ($E_{cut\text{-}off}$), where $E_{cut\text{-}off}$ is the intersection of the high-binding-energy edge with the baseline[44]. And the difference between valence band maximum (E_{VB}) and E_F is calculated by the intersection with baseline in the low binding energy region[45]. Then the conduction band minimum (E_{CB}) can be calculated by E_{VB} and bandgap. As calculated from the high and low energy cutoff regions shown in Figure 3g and 3h, the work functions are 4.62 eV, 4.52 eV, 4.49 eV, 4.42 eV and 4.73 eV for the perovskite film with n-OAI, tert-OAI, tert-OABr, tert-OACl passivation and pristine film; this is related to the charge redistribution after passivation. The E_{VB} of perovskite films are 5.88 eV, 5.76 eV, 5.85 eV, 5.54 eV and 5.98 eV after n-OAI, tert-OAI, tert-OABr, tert-OACl and without passivation, respectively.

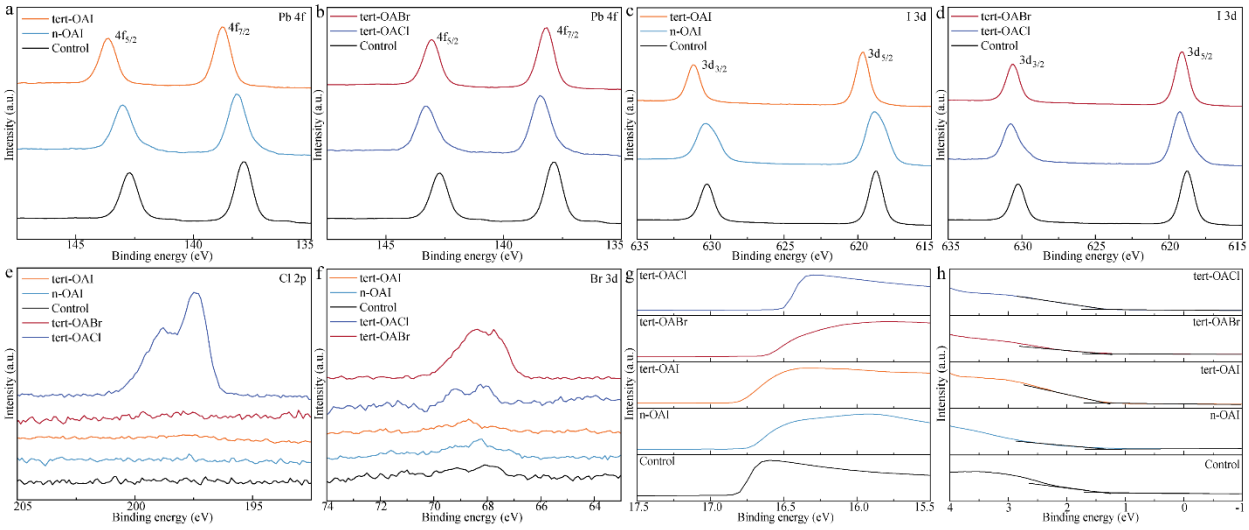

Figure 3 a-b. The XPS-Pb spectra of perovskite films with tert-OAI, n-OAI (a), and with tert-OABr and tert-OACl (b); c-d. The XPS-I spectra of perovskite films with tert-OAI, n-OAI (c), and with tert-OABr and tert-OACl (d); e. The XPS-Cl spectra of perovskite films with and without passivation; f. The XPS-Cl spectra of perovskite films with and without passivation; g-h. The high and low cutoff regions of UPS spectra of perovskite films with and without passivation layers.

The E_{VB} and E_{CB} of perovskite films have different energy shifts after passivation, which could create a built-in electric field, as shown in Figure S8. The energy level shifting of perovskite films with passivation layers due to the 2D/3D perovskite heterojunctions formed[46,47]. And the 2D perovskite always exhibits a higher work function than 3D perovskite, leading to band bending at the interface between perovskite films and passivation layers and influencing the efficiency of devices[48]. In addition, the different shifts of E_F of perovskite with passivation layers could be explained by the influence of dipole moment for passivation materials (n-OAI, tert-OAI, tert-OABr, and tert-OACl)[48].

Based on the above results, the tert-OAI exhibits a better passivation effect on PSCs than tert-OACl, tert-OABr, and n-OAI. To further investigate the different material passivation effects on the devices, density functional theory (DFT) calculations were carried out. The $FAPbI_3$ perovskite structure is used as a simplified model in the calculation, which is the major component of our PSCs. The DFT calculations utilized Perdew−Burke−Ernzerh generalized gradient approximation (PBE-GGA) simulations on a 2 × 2 × 2 cubic perovskite supercell in the exposed (100) surface. The trap and defects within the perovskite bulk and on the surface of the perovskite films are unfavorable for carrier extraction and transfer, while the defects on the perovskite surface could easily generate deeper defect states[49]. Hence, the three typical vacancy defects in perovskite films are considered and discussed here, including the organic cation, lead, and iodide vacancies (V_{FA}, $V_{Pb,}$ and V_I)[49,50]. The projected density of states (PDOS) and electron charge difference density are investigated, which may insight into the passivation influence of different halogen atoms, linear-alkyl-chain, and branched-alkyl-chain of ammonium salts on V_{FA}, $V_{Pb,}$ and V_I of perovskite surface. The different halogen ions (Br^-, Cl^-, and I^-) are located on the surface of perovskite films with V_I, and entire structures are optimized for energy minimization. The PDOS of perovskite with halogen ions passivation are shown in Figures 4a to 4c, which discuss three passivation conditions,

including halogen ions on the surface of perovskite with V_I (Figure 4a), halogen ions completely filling V_I (Figure 4b) and halogen ions partially filling V_I (Figure 4c). After introducing the halogen ions onto the perovskite surface, the perovskite lattice structure, the periodic potential within perovskite, the distribution of electrons, and the hybridization of I and Pb orbitals are slightly changed, which further influence the bandgap and the trap state of perovskite films[49]. To study the influence of different halogen ions on the PDOS of perovskite films, the perovskite film with I^- shows fewer trap states at valance band maximum (VBM) in the two conditions: 1) halogen ions on the surface of perovskite films with V_I and 2) the halogen ions completely filling the V_I on the perovskite film surface. And the perovskite films with I^- and Cl^- present similar trap states in the condition of halogen ions partially filling V_I in comparison to Br^-. Thus, the I^- ions are suitable for passivating V_I in the perovskite surface, whether the halogen ions fill into the perovskite lattice or hang on the surface of perovskite films. The influence of the alkyl-chain part of ammonium salts on the PDOS of perovskite films with V_{FA}, $V_{Pb,}$ and V_I are also investigated. It is clear to observe the trap states of perovskite films are largely shallowed near conduction band minimum (CBM) and VBM after the films with V_{FA} and V_{Pb} passivated by alkyl-chain in Figures 4e and 4f, while the PDOS of perovskite with V_I does not show much difference in Figure 4g. Especially, the perovskite films with V_{Pb} present less trap density after branched-alkyl chain passivation than linear-alkyl chain passivation near VBM and CBM. The branched-alkyl chain and linear-alkyl chain passivation on perovskite films with V_{FA} and V_I exhibits a similar passivation effect on the PODS of perovskite films. Therefore, the branched-alkyl chain shows a better passivation effect on V_{Pb} of perovskite films, which means V_{Pb} of perovskite films preferred branched-alkyl chain ammonium salt passivation than the linear-alkyl-chain one.

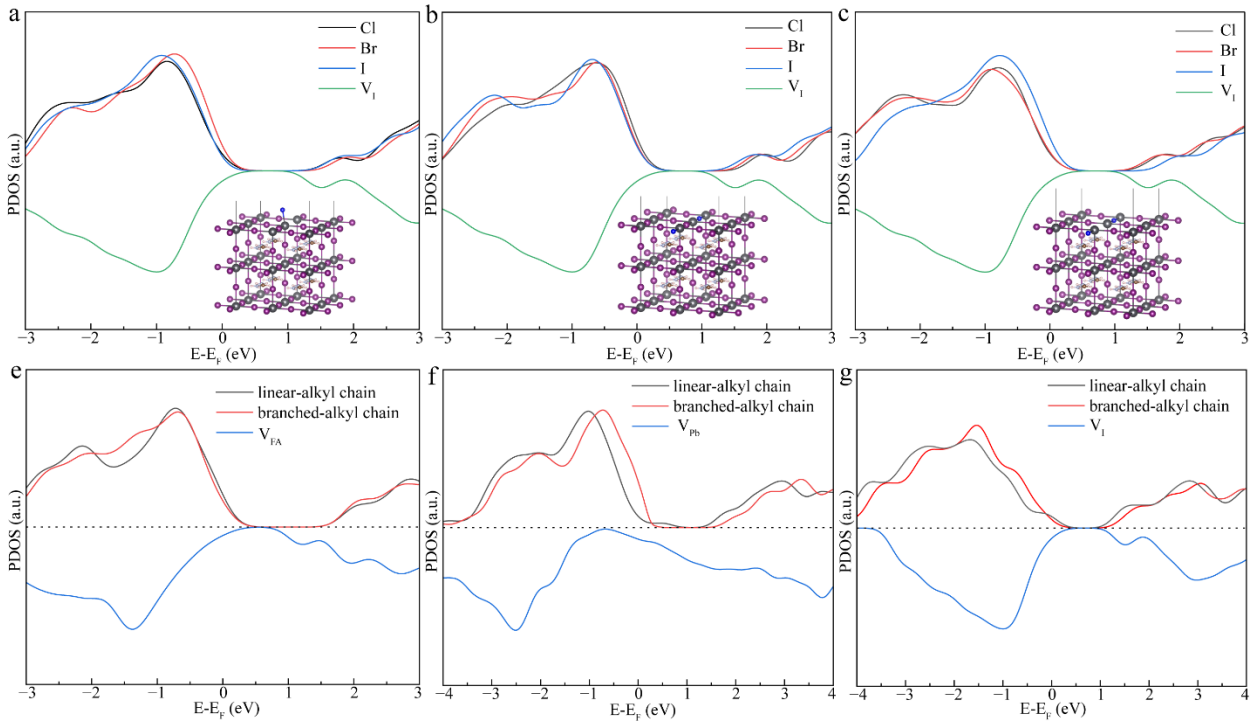

Figure 4 a. The PDOS of halogen ions on the surface of perovskite films with VI; b. The PDOS of halogen ions completely fill the V_I in the perovskite films; c. The PDOS of halogen ions partially fill the V_I in the perovskite films; e-g. The PDOS of perovskite films with V_{FA}(e), V_{Pb}(f) and V_I(g) after linear-alkyl chain and branched-alkyl chain passivation.

The improved charge transport after ammonium salt passivation and the chemical interaction between the ammonium salts and perovskite films motivated us to study the influence of the change in basic properties on the performance of PSCs. The n-i-p planar heterojunction structure PSCs are fabricated with the structure of FTO glass/ TiO_2/perovskite/tert-OAI (tert-OACl, tert-OABr and n-OAI)/Spiro-MeOTAD/Au. The perovskite absorber layer is sandwiched between the electron transport layer (TiO_2) and hole transport layer (Spiro-MeOTAD). The photoelectrons from the perovskite layer transfer to the TiO_2 layer and FTO substrates, while the hole carriers transfer to the Spiro-MeOTAD layer and finally reach Au electrode. The photovoltaic parameters distribution (PCE, J_{sc}, V_{oc}, and FF) of PSCs with and without passivation are shown in Figure 5a to 5d. The control devices exhibit an average PCE of ~22.23 % with a short-circuit current density (J_{sc}) of ~24.77 mA/cm^2, an open-circuit voltage (V_{oc}) of ~1.14 V, and a fill factor (FF) of ~79.06 %. The performance of the tert-OAI modified devices shows an average PCE of ~24.11% with a J_{sc}

of ~24.92 mA/cm^2, a V_{oc} of ~1.18 V and an FF of ~81.83%. The efficiency of devices increases from 22.23% to 24.11 % after tert-OAI passivation, benefiting from over the 40 mV V_{oc} improvement. The average PSCs modified by tert-OABr, tert-OACl, and n-OAI also present significant improvements in J-V performance, with the average PCE increasing to 22.66 %, 23.24 %, and 23.25 %, respectively, and the detailed parameters are shown in Table S1. The performance of PSCs is successively enhanced by n-OAI, tert-OABr, tert-OACl, and tert-OAI. Therefore, the passivation effect of the alkyl chain architecture in ammonium salts is more significant than that of the halogen atom, with devices passivated by branched architectures demonstrating superior performance compared to those with linear architectures. Figure 5e exhibits J-V curves of the champion devices passivated by different ammonium salts, and the detailed values of J-V performance are shown in Table S2. The champion devices with linear-alkyl-chain (n-OAI) exhibit a PCE of 23.84% with V_{oc} of 1.16V, which is increased from the PCE of 23.17% with the V_{oc} of 1.15 V of the champion device without passivation. By contrast, the PSCs with branched-alkyl-chain of tert-OAI, tert-OACl, and tert-OABr passivated present the V_{oc} of 1.19 V, 1.17 V, and 1.17 V, and the PCE of 25.49%, 24.88% and 24.19% respectively, which shows increased PCE with remarkable V_{oc} enhancement. The parameters of J-V performance for PSCs with treatments are shown in Table S2. To further investigate the passivation effects on the devices, the forward and reversed scanned J-V curves of devices with different materials are exhibited in Figure S9, and the detailed J-V values are also provided in Table S3. The hysteresis index (HI) is believed to be caused by ion migration and accumulation at interfaces between perovskite and charge transport layers, HI can be calculated using Equation (1)[51,52].

$$HI = \frac{PCE_R - PCE_F}{PCE_R} \quad (1)$$

The calculated HI of the devices passivated by n-OAI, tert-OABr, tert-OACl, and tert-OAI are 0.0118, 0.00697, 0.00789, and 0.00618, respectively. The results suggest that the HI of devices with passivation significantly improved from 0.0319 for the PSCs without passivation, indicating that the passivation layer decreases ion accumulation and enhances the charge carrier transport between the perovskite layer and the hole transport layer. In addition, Figure S10 presents the tracking of the maximum power point (MPP) of PSCs current and PCE with and without interfacial passivation for 400 s. The stabilized power output current of the pristine device is around 23.46 mA/cm^2 for 400 s, which decreases from the initial current of around 25.52 mA/cm^{2,} and the

current loss is around 8.07%. The stabilized current of devices passivated by n-OAI, tert-OABr, tert-OACl, and tert-OAI are 25.02 mA/cm^2, 24.90 mA/cm^2, 25.15 mA/cm^2 and 25.34 mA/cm^2, which keep the 97.82%, 99.92%, 99.88% and 99.89%, respectively, of the initial current. Therefore, the stabilized PCE of devices with n-OAI, tert-OABr, tert-OACl, and tert-OAI are 23.02%, 23.42%, 23.65%, and 24.07% with voltage of 0.92V, 0.94V, 0.94V and 0.95V, which exhibit the significant improvement stabilized PCE from 21.34% with 0.91V of the pristine device. These results suggest that the charge carrier extraction and transport have been improved after interfacial passivation, which is consistent with the different scan directions of the J-V curve results. The incident photon to electron conversion efficiency (IPCE) spectra and the integrated current are shown in Figure 5f. The devices with n-OAI and tert-OAI exhibit higher response from 300 nm to 850 nm than the pristine device, and the corresponding integrated current is 24.03 mA/cm^2 and 24.22 mA/cm^2 compared to 23.66 mA/cm^2 for the control device (Figure S11). The difference between the integrated current from EQE spectra and the J_{sc} from J-V curves is within 5%, so the integrated current density of the devices obtained by EQE is consistent with J_{sc} obtained from J-V measurements.

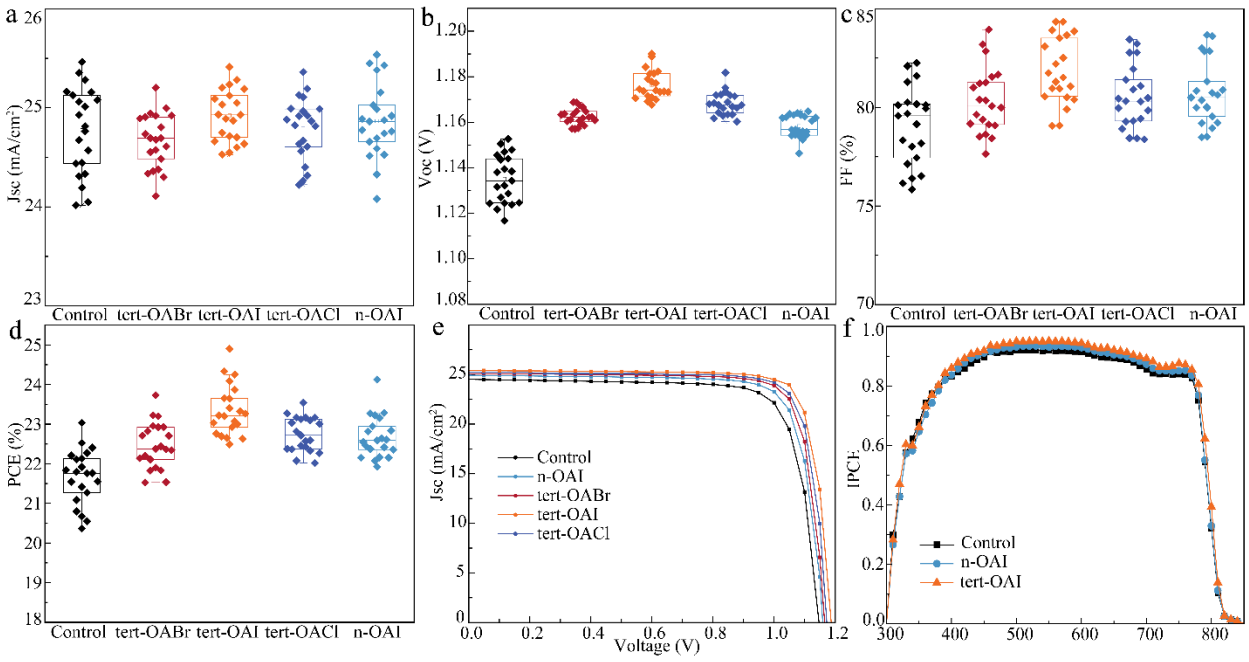

Figure 5 a-d. The distributions of device performance with and without passivation: J_{sc}(a), V_{oc} (b), FF(c) and PCE (d); e. The J-V curves of the champion device with and without passivation; f. The IPCE curves of devices with and without passivation.

To investigate the passivation effects of linear and branched alkyl-chain ammonium salts on devices with V_{Pb} and V_{FA} defects, the devices were fabricated by reducing the PbI_2 and FAI concentrations in the perovskite precursor solution. Figure S12 presents the parameters (J_{sc}, V_{oc}, FF and PCE) of the PSCs-V_{Pb} with tert-OAI, n-OAI, and without passivation. And the detailed parameters of devices with V_{FA} are shown in Figure S13. These results are further confirmed by the previously discussed DFT calculations result.

To further study the passivation influence on the devices, the Mott-Schottky (M-S) curves were measured and presented in Figure 6a. The built-in potential (V_{bi}) of PSCs with and without passivation are observed from the intercept of the M-S curves under dark conditions, and the V_{bi} values of devices with tert-OAI, n-OAI, tert-OABr, tert-OACl, and control are 0.88 V, 0.85 V, 0.84 V, 0.837 V and 0.79V, respectively. The device with tert-OAI modification exhibits higher V_{bi} and smaller currents, which suggests lower current leakage and less non-radiative recombination and Voc and FF enhancement of PSCs[53]. The trap density of states (tDOS) of the devices with and without passivation is calculated by Equation (2)[54,55],

$$N_{tDOS} = \frac{-\omega V_{bi}}{qkTW}\frac{dC}{d\omega} \quad (2)$$

where ω and T are the angular frequency and the absolute temperature, respectively, q is the electron charge (1.60×10^{-19} C), and k is the Boltzmann constant (1.38×10^{-23} J/K). The tDOS values of PSCs with tert-OAI and n-OAI passivation are illustrated in Figure 6b. V_{bi} is the built-in potential calculated from the M-S curves (Figure 6a), and W is the depletion region thickness [56,57]. The tDOS value of the device with tert-OAI is lower than that of n-OAI in the range from 0.40 eV to 0.65 eV. The results indicate the device with tert-OAI has fewer traps and defects in both shallow and deep regions, which further influence the PCE of the devices[58]. To further investigate the defect density, the space charge limited current (SCLC) curves are measured. The SCLC curves are obtained by the J-V testing method of the hole-only and devices with a configuration of FTO/PTAA/Perovskite with and without passivation/Spiro-OMeTAD/Au and electron-only devices of FTO/TiO_2/Perovskite/$PC_{60}BM$/Au structure, as presented in Figure 6c and 6d. The SCLC curves are divided into three regions, including the ohmic region (slope = 1), trap-free region (slope = 2), and trap limit region[59], and the turning points at the trap limit region and ohmic

region in the curves are the trap limit voltage (V_{TFL}) values. The V_{TFL} value of the control device is 0.70 V, which decreases to 0. 55 V, 0.57 V, 0.60 V, and 0.63 V after the tert-OAI, tert-OACl, tert-OABr, and n-OAI passivation respectively. The calculated corresponding hole trap of PSCs are 8.35 x 10^{15} cm^{-3}, 8.61 x 10^{15} cm^{-3}, 9.10 x 10^{15} $cm^{-3,}$ and 9.66 x 10^{15} cm^{-3} for devices with tert-OAI, tert-OACl, tert-OABr and n-OAI passivation respectively, which are all lower than the control device of 1.06 x 10^{16} cm^{-3}. In addition, for the electron-only devices, the V_{TFL} values for the devices passivated by tert-OAI, tert-OACl, tert-OABr, n-OAI, and the device without passivation are 0.47 V, 0.61 V, 0.62 V, 0.68 V and 0.80V, respectively. The corresponding electron defect density of devices are 7.10 x 10^{15} cm^{-3}, 9.17 x $10^{15}cm^{-3}$, 9.28 x 10^{15} cm^{-3}, 1.04 x 10^{16} cm^{-3} and 1.21 x 10^{16} cm^{-3}, respectively. These results reveal that the hole and electron defect density of PSCs is decreased by passivation, especially with the tert-OAI passivation. Therefore, the defect-induced non-radiative recombination would be reduced, and the efficient charge carrier extractions would be improved[60]. To study the passivation influence on charge recombination and extraction, the V_{oc} values with various light intensity curves are measured, and the diode ideality factor (n) of devices was determined by the slope of the curves in Figure 6e[61]. The slopes of V_{oc}-light intensity curves for the devices with tert-OAI, tert-OACl, tert-OABr, n-OAI, and without passivation are 1.57 kT/e, 1.89 kT/e, 1.82 kT/e, 1.89 kT/e and 1.99 kT/e, respectively, where T is the temperature (K), k is the Boltzmann constant (1.38×10^{-23} J/K), and q is the elementary charge (1.60×10^{-19} C). The trap-assisted monomolecular recombination is in a dominant contribution when the slope is close to 2kT/e. Therefore, the device with tert-OAI has less trap-assisted recombination than the devices with other passivation, consistent with J-V results[62,63]. In addition, less charge recombination is also related to charge transfer and collection; therefore, the non-radiative and charge transport loss in FF is calculated using Equations (3) and (4)[64],

$$FF_{max} = \frac{\upsilon_{oc} - \ln(\upsilon_{oc} + 0.72)}{\upsilon_{oc} + 1} \quad (3)$$

$$\upsilon_{oc} = \frac{V_{oc}}{nKT} \quad (4)$$

where K is the Boltzmann constant; T is the temperature, and n is the diode ideality factor[64]. As presented in Figure 6f, the non-radiative loss of the devices with tert-OAI and n-OAI are obviously suppressed, while the device with tert-OAI shows lower non-radiative recombination loss.

Therefore, the tert-OAI passivation for the PSCs not only decreases the non-radiative recombination but also enhances the charge carrier transfer in the PSCs[65].

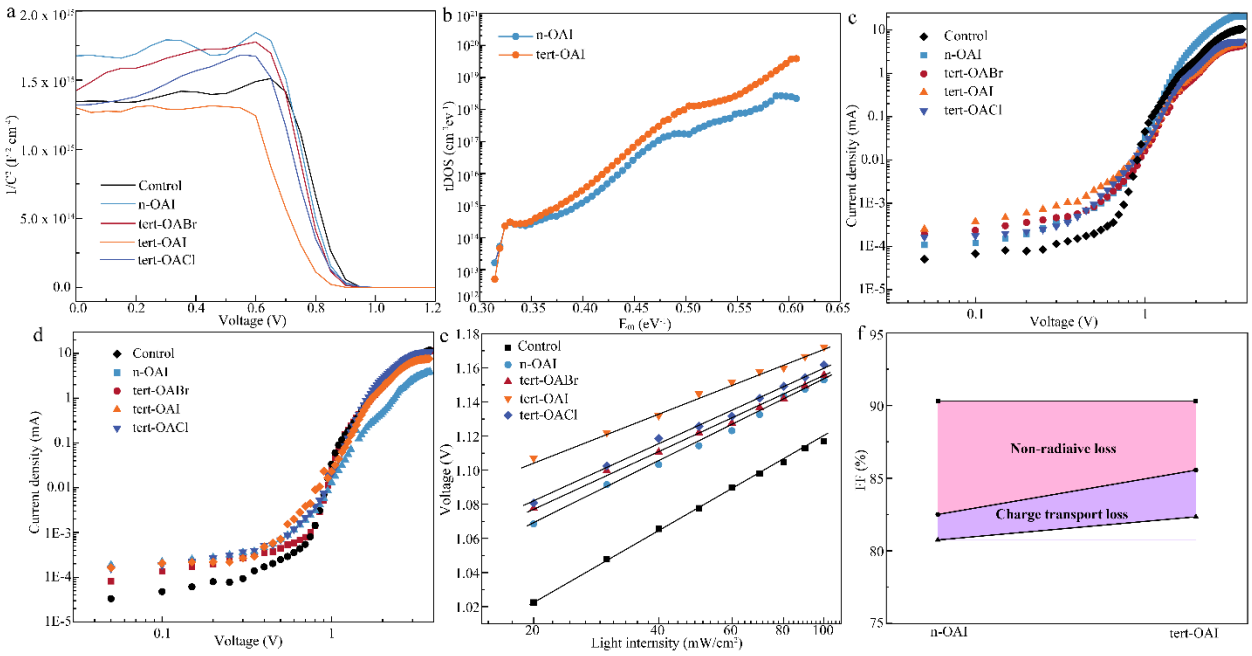

Figure 6 a. The Mott-Schottky (M-S) curves of perovskite films; b. The tDOS of devices with tert-OAI and n-OAI; c-d. The hole and electron-only devices with and without passivation; e. The dependency of V_{OC} on the light intensity of the devices with and without passivation; f. The FF loss analysis of the devices with tert-OAI and n-OAI.

The dark J-V curves of the devices with and without passivation are measured to study the charge carrier transportation. In Figure 7a, the dark J-V curves are divided into three regions (I, II, and III) by different voltages related to the leakage (shunt) current region, diode space-charge region, and diffusion current region[66]. The devices with tert-OAI exhibit a lower leakage current in region I than the other devices, indicating that the tert-OAI passivation minimizes the traps and defects at the interface between perovskite and hole transport layers[67]. The series resistance of the devices is related to the current in Region III. The devices with tert-OAI exhibit the lowest current, suggesting that the tert-OAI modification reduces the series resistance and enhances the charge carrier transport[68]. Furthermore, region II reveals the charge recombination in the devices, and the slope of the J-V dark curves in Region II is related to the inverse values of R_{sh}. The reverse

saturation current (J_0) is the intercept of the linear fit curves at voltage 0 V, and the relationship between J_0 and V_{oc} of PSCs can be expressed by Shockley Equation (5)[69],

$$V_{oc} = \frac{nKT}{q} ln \frac{J_{sc}}{J_0} \quad (5)$$

where n is the ideality factor, K is the Boltzmann constant, T is the absolute temperature, q is the elementary charge, J_{sc} is the photogenerated short-circuit current, and J_0 is the reverse saturation current. The PSCs with tert-OAI modification show lower J_0 than those with and without other passivation, so the device with tert-OAI passivation shows higher V_{oc} in the photogenerated J-V curves. Electrochemical impedance spectroscopy (EIS) is carried out to further investigate the charge carrier extraction and transport. The Nyquist curves of the devices with and without passivation under dark conditions are exhibited in Figure 7b, and the equivalent circuit diagram is shown in the inset. The series resistance of PSCs can be expressed by R_s, which is ohmic resistance due to the connecting resistance[70,71]. R_s values of the device with tert-OAI and n-OAI passivation are 22.49 Ω and 63.50 Ω, respectively, which are lower than the control device of 79.27 Ω. The Nyquist curves are composed of two semicircles; the semicircle in the low frequency is related to the recombination resistance (R_{rec}), while the high-frequency semicircle corresponds to the charge transfer resistance (R_{ct})[72]. Compared to the device with and without other passivation, the higher R_{rec} values of the device with tert-OAI indicate the lower charge recombination at the interface between different layers[73,74]. Therefore, the branched-alkyl-chain materials have better passivation effects on the device performance than the linear-alkyl-chain materials. For the X atom (I, Br, and Cl) in the perovskite structure (ABX_3), the I^- passivation influence on the trap and defects in the perovskite film is more efficient.

The femtosecond transient absorption (fs-TA) spectra of perovskite films with and without passivation are performed under 400 nm excitation to investigate recombination kinetics, as presented in Figure 7c to 7e. The ground state bleach signal appears at 776 nm due to the photogenerated Wannier-Mott type excitons, consistent with the absorption onset in the UV-vis absorption spectra. At early delay times (0.5 ps), the bleach peak is asymmetric with a tail on the blue side in all perovskite films, which is attributed to the hot carriers generated by the above band gap excitation[75]. At 1-10 ps, the bleach signals in all the samples show negligible changes, indicating no ultrafast carrier trapping at < 10 ps. However, at > 30 ps, the pristine perovskite and the n-OAI passivated perovskite show faster bleach recovery compared to the tert-OAI passivated

one, suggesting a better passivation effect enabled by the branched-alkyl chain ammonium. Comparison of the bleach kinetics in Figure 7f further confirms this conclusion, where the kinetics of the pristine and n-OAI passivated samples decay faster. The TA data for the tert-OACl and tert-OABr passivated samples are provided in Figure S14, showing similar bleach recovery compared to the tert-OAI passivated sample. The TA decay kinetics are fit by the single exponential decay function, resulting in the lifetime constant of 2.8 ± 0.2, 3.8 ± 0.3, 5.0 ± 0.4, 5.3 ± 0.5, and 4.5 ± 0.4 ns for the pristine, n-OAI passivated, tert-OAI passivated, tert-OACl passivated, and tert-OABr passivated samples, respectively. We note that the similar passivation effects of tert-OAI, tert-OABr, and tert-OACl at the < 2 ns time window are contrast to the PL decay kinetics in Figure S15 in the microsecond time scales. These results may suggest that I^- is better for passivating trap states which cause slow carrier trapping, while different halogen anions are insensitive to other traps that affect the nanosecond carrier dynamics.

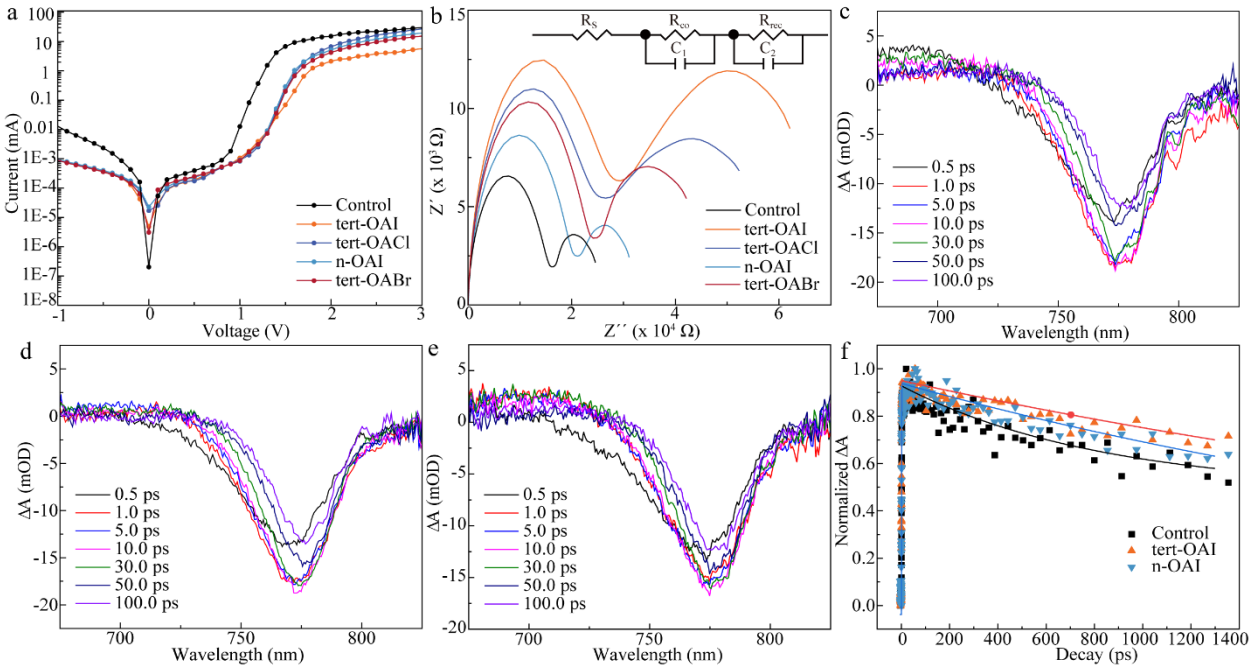

Figure 7 a. The J-V dark curves of devices with and without passivation; b. The EIS spectra of devices with and without passivation; c-e. The TA spectra of perovskite films without passivation (c), with n-OAI (d) and tert-OAI (e); f. The normalized TA kinetics (averaged from 774 nm to 777 nm) of the pristine (black squares), tert-OAI passivated (orange triangles), and n-OAI passivated (blue triangles) perovskite films.

To study the optical characteristics of perovskite films with and without passivation and charge carrier recombination dynamics of PSCs, UV-vis absorption spectroscopy, the steady-state photoluminescence (PL), the Electroluminescence (EL) spectra and the time-resolved photoluminescence (TRPL) decay kinetics were carried out, as presented in Figure S15. To further understand the passivation effect on the charge transport and recombination of devices, the Nyquist plots of devices with tert-OAI and n-OAI passivation are measured with different applied biases in the dark (Figure S16).

To further study the passivation influence of tert-OAI on the PSCs stability, the unencapsulated devices were measured for long-term (ISOS-D-1) and thermal (ISOS-D-2) stability. As indicated in Figure 8a, the device with tert-OAI passivated retains over 85% of the initial efficiency after 1000 h under N_2 at room temperature, and the control device only shows around 81% retention of initial efficiency. Furthermore, Figure 8b exhibits the thermal stability of devices with and without tert-OAI passivation, the unencapsulated devices were kept under 85 ℃ under N_2. Devices with tert-OAI passivation retained 63% of their initial PCE after approximately 500 hours, compared to only 53% for the control devices. The perovskite film is sensitive to moisture, which is the main reason for the performance decay. And the detailed decay steps in the presence of moisture can be explained by the following reactions[76]. The perovskite films would decompose into I_2 and produce the iodine vacancies, which are detrimental to the device long-term performance[77–79].

$$CH(NH_2)_2PbI_3(S) \overset{H_2O}{\longleftrightarrow} PbI_2(s) + CH(NH_2)_2I\ (aq) \quad (6)$$

$$CH(NH_2)_2I(aq) \leftrightarrow CH(NH_2)_2(aq) + HI(aq) \quad (7)$$

$$HI(aq) \leftrightarrow H_2 + I_2 \quad (8)$$

Figure S17 exhibits the UV-vis absorption of I_2 solution and I_2 solution with tert-OAI. There are two absorption peaks of I_2 solution at ~450 nm and ~360 nm, attributed to absorption of I_2 and I_3^- [80–82]. And the I_2 solution with tert-OAI only shows the I_3^- peak at 360 nm, which indicates I_2 has been changed to I_3^- by tert-OAI. Therefore, the passivation material tert-OAI can change I_2 to I_3^- and modify the iodine vacancies in the films, which further influences the long-term stability of devices.

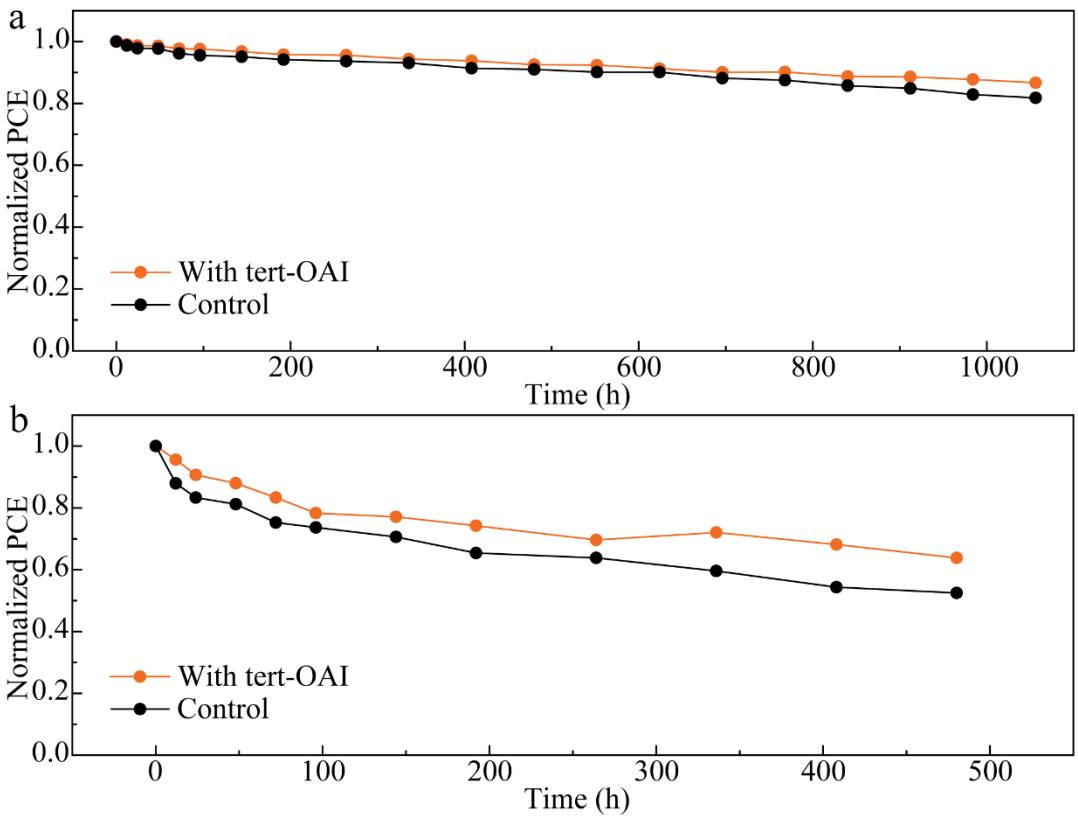

Figure 8 The long-term stability(a) and thermal stability(b) of devices with and without tert-OAI passivation

3. Conclusions

In summary, we utilized four ammonium salts with different alkyl chains and halogen ions to passivate the surface of perovskite films by interface passivation. Our comparison of passivation effects revealed that the alkyl chain in the ammonium salts plays a more decisive role in passivation than the halogen ions. XPS, FTIR, XRD, and electron-only device measurements confirmed the passivation effects on the perovskite films. Furthermore, we applied DFT calculations to understand the passivation mechanism of the different defect types of perovskite films.

Our findings indicate that halogen ions are effective in passivating V_I defects, with I^- ions reducing defect density more effectively than Cl^- or Br^- ions, as confirmed by device performance. For V_{Pb} and V_{FA} defects, branched-alkyl chain ammonium salts demonstrated superior passivation effects compared to linear-alkyl chain salts. PSCs with tert-OAI achieved an impressive efficiency of 25.49%, with a V_{oc} of 1.19 V, a J_{sc} of 25.40 mA/cm², and an FF of 84.34%. Furthermore, devices with tert-OAI retained over 85% of their initial PCE values after 1000 h under N_2. This work

provides a targeted passivation strategy for PSCs using tailored alkyl-chain and halogen ions to address specific defect types in perovskite films, offering a pathway to enhanced performance and stability.

Supporting information

Supporting Information is available from the Wiley Online Library or from the author.

Acknowledgements

This work was supported by the National Science Foundation (OIA-2418390). The ultrafast spectroscopy measurement is supported by the National Science Foundation (OIA-2326788). The steady-state PL and TRPL are supported by the National Science Foundation (Award#1900047). S. U. and X. G. thank NSF grant OIA-1757220 for providing financial support for 2D GIWAXS measurements. Y. Q is partially supported by NSF grant DMR-2242467. I. J. is supported by NSF-PREM grant (NSF-PREM-2423854). J. G. is supported by the Department of Energy Historically Black Colleges and Universities (HBCU) Clean Energy Education Prize. K. W. acknowledges partial financial support from U.S. Department of Energy, Basic Energy Sciences (Award No. DE-SC0024924) for AFM imaging and surface potential measurements. T. L. acknowledges support from the National Science Foundation (CHE-2305112). ToF-SIMS analyses were carried out with support provided by the National Science Foundation CBET-1626418. This work was conducted in part using resources of the Shared Equipment Authority at Rice University.

Conflict of interest

The authors declare no conflict interest.

Data Availability Statement

The data that support the findings of this study are available from the corresponding author upon reasonable request.

Received: ((will be filled in by the editorial staff))
Revised: ((will be filled in by the editorial staff))
Published online: ((will be filled in by the editorial staff))

References

[1] L. Zhu, X. Zhang, M. Li, X. Shang, K. Lei, B. Zhang, C. Chen, S. Zheng, H. Song, J. Chen, *Adv Energy Mater* **2021**, *11*, 2100529.

[2] "NREL," can be found under https://www.nrel.gov/pv/cell-efficiency.

[3] K. Wang, L. Zheng, Y. Hou, A. Nozariasbmarz, B. Poudel, J. Yoon, T. Ye, D. Yang, A. V Pogrebnyakov, V. Gopalan, S. Priya, *Joule* **2022**, *6*, 756.

[4] S. Wang, Y. Jiang, E. J. Juarez-Perez, L. K. Ono, Y. Qi, *Nat Energy* **2016**, *2*, DOI 10.1038/nenergy.2016.195.

[5] L. Shi, M. P. Bucknall, T. L. Young, M. Zhang, L. Hu, J. Bing, D. S. Lee, J. Kim, T. Wu, N. Takamure, D. R. McKenzie, S. Huang, M. A. Green, A. W. Y. Ho-Baillie, *Science (1979)* **2020**, *368*, DOI 10.1126/science.aba2412.

[6] J. Wu, J. Shi, Y. Li, H. Li, H. Wu, Y. Luo, D. Li, Q. Meng, *Adv Energy Mater* **2019**, *9*, DOI 10.1002/aenm.201901352.

[7] J. Chen, N.-G. Park, *ACS Energy Lett* **2020**, *5*, 2742.

[8] D. Luo, R. Su, W. Zhang, Q. Gong, R. Zhu, *Nat Rev Mater* **2019**, *5*, 44.

[9] C. M. Wolff, P. Caprioglio, M. Stolterfoht, D. Neher, *Advanced Materials* **2019**, *31*, DOI 10.1002/adma.201902762.

[10] J. Chen, S. Kim, N. Park, *Advanced Materials* **2018**, *30*, DOI 10.1002/adma.201801948.

[11] Y. Li, H. Wu, W. Qi, X. Zhou, J. Li, J. Cheng, Y. Zhao, Y. Li, X. Zhang, *Nano Energy* **2020**, *77*, 105237.

[12] J. Zhang, X. Niu, C. Peng, H. Jiang, L. Yu, H. Zhou, Z. Zhou, *Angewandte Chemie* **2023**, *135*, DOI 10.1002/ange.202314106.

[13] Z. He, Z. Zhang, J. Ding, W. Gao, M. Li, C. Chen, *Small* **2024**, *20*, DOI 10.1002/smll.202404334.

[14] S. Liu, Z. Sun, X. Lei, T. Miao, Q. Zhou, R. Chen, J. Wang, F. Ren, Y. Pan, Y. Cai, Z. Tan, W. Liu, X. Liu, J. Li, Y. Zhang, B. Xu, Z. Liu, W. Chen, *Advanced Materials* **2024**, DOI 10.1002/adma.202415100.

[15] P. Zhao, J. Subbiah, B. Zhang, J. A. Hutchison, G. Ahluwalia, V. Mitchell, K. P. Ghiggino, D. J. Jones, *Adv Mater Interfaces* **2023**, *10*, DOI 10.1002/admi.202202313.

[16] L. Zheng, L. Shen, Z. Fang, P. Song, W. Tian, J. Chen, K. Liu, Y. Luo, P. Xu, J. Yang, C. Tian, L. Xie, Z. Wei, *Adv Energy Mater* **2023**, *13*, DOI 10.1002/aenm.202301066.

[17] Y. Wu, Q. Wang, Y. Chen, W. Qiu, Q. Peng, *Energy & Environmental Science* **2022**, *15*, 4700.

[18] S. Liu, X. Guan, W. Xiao, R. Chen, J. Zhou, F. Ren, J. Wang, W. Chen, S. Li, L. Qiu, Y. Zhao, Z. Liu, W. Chen, *Adv Funct Mater* **2022**, *32*, DOI 10.1002/adfm.202205009.

[19] M. M. Osman, A. M. El-naggar, A. Q. Alanazi, A. M. Aldhafiri, A. A. Albassam, *Nanomaterials* **2023**, *13*, DOI 10.3390/nano13091492.

[20] H. Lee, Y. Kang, S. Kwon, D. Kim, S. Na, *Small Methods* **2023**, *8*, DOI 10.1002/smtd.202300948.

[21] T. Duong, H. Pham, Y. Yin, J. Peng, M. A. Mahmud, Y. Wu, H. Shen, J. Zheng, T. Tran-Phu, T. Lu, L. Li, A. Kumar, G. G. Andersson, A. Ho-Baillie, Y. Liu, T. White, K. Weber, K. Catchpole, *J Mater Chem A Mater* **2021**, *9*, 18454.

[22] S. Y. Kwon, B. Kang, J. H. Won, C. Y. Lee, K. Hwang, H. H. Kim, D. Park, W. K. Choi, I. S. Kim, G. Y. Kim, Y. H. Jang, P. Lee, S. H. Im, T. Kim, *Adv Mater Interfaces* **2023**, *10*, DOI 10.1002/admi.202202249.

[23] K. Hisatsune, S. Uchida, T. N. Murakami, A. Kogo, *ACS Appl Energy Mater* **2024**, *7*, 5315.

[24] Y. Feng, R. Liu, F. Li, M. Jin, Q. Du, Y. Rong, H. Hu, M. Wang, Y. Li, Z. Shen, Y. Liu, H. Li, C. Chen, *J Mater Chem C Mater* **2022**, *10*, 12699.

[25] J. Lim, A. I. Rafieh, N. Shibayama, J. Xia, J.-N. Audinot, T. Wirtz, S. Kinge, S. W. Glunz, Y. Ding, B. Ding, H. Kim, M. Saliba, Z. Fei, P. J. Dyson, M. K. Nazeeruddin, H. Kanda, *Energy & Environmental Science* **2024**, *17*, 8209.

[26] T. Ji, Y. Cao, D. Lin, M. Stolar, C. P. Berlinguette, *ACS Appl Energy Mater* **2024**, *7*, 5371.

[27] J. Pan, Z. Chen, T. Zhang, B. Hu, H. Ning, Z. Meng, Z. Su, D. Nodari, W. Xu, G. Min, M. Chen, X. Liu, N. Gasparini, S. A. Haque, P. R. F. Barnes, F. Gao, A. A. Bakulin, *Nat Commun* **2023**, *14*, DOI 10.1038/s41467-023-43852-5.

[28] T. Chen, J. Xie, B. Wen, Q. Yin, R. Lin, S. Zhu, P. Gao, *Nat Commun* **2023**, *14*, DOI 10.1038/s41467-023-41853-y.

[29] G. Yang, Z. Ni, Z. J. Yu, B. W. Larson, Z. Yu, B. Chen, A. Alasfour, X. Xiao, J. M. Luther, Z. C. Holman, J. Huang, *Nat Photonics* **2022**, *16*, 588.

[30] Z. Liang, Y. Zhang, H. Xu, W. Chen, B. Liu, J. Zhang, H. Zhang, Z. Wang, D.-H. Kang, J. Zeng, X. Gao, Q. Wang, H. Hu, H. Zhou, X. Cai, X. Tian, P. Reiss, B. Xu, T. Kirchartz, Z. Xiao, S. Dai, N.-G. Park, J. Ye, X. Pan, *Nature* **2023**, *624*, 557.

[31] G. Liu, H. Zheng, L. Zhang, H. Xu, S. Xu, X. Xu, Z. Liang, X. Pan, *Chemical Engineering Journal* **2021**, *407*, 127204.

[32] G. Liu, H. Zheng, H. Xu, L. Zhang, X. Xu, S. Xu, X. Pan, *Nano Energy* **2020**, *73*, 104753.

[33] Y. Yang, J. Wu, X. Wang, Q. Guo, X. Liu, W. Sun, Y. Wei, Y. Huang, Z. Lan, M. Huang, J. Lin, H. Chen, Z. Wei, *Advanced Materials* **2019**, *32*, DOI 10.1002/adma.201904347.

[34] C.-S. Jiang, M. Yang, Y. Zhou, B. To, S. U. Nanayakkara, J. M. Luther, W. Zhou, J. J. Berry, J. van de Lagemaat, N. P. Padture, K. Zhu, M. M. Al-Jassim, *Nat Commun* **2015**, *6*, DOI 10.1038/ncomms9397.

[35] G. Li, J. Song, J. Wu, Z. Song, X. Wang, W. Sun, L. Fan, J. Lin, M. Huang, Z. Lan, P. Gao, *ACS Energy Lett* **2021**, *6*, 3614.

[36] I. S. Zhidkov, D. W. Boukhvalov, A. F. Akbulatov, L. A. Frolova, L. D. Finkelstein, A. I. Kukharenko, S. O. Cholakh, C.-C. Chueh, P. A. Troshin, E. Z. Kurmaev, *Nano Energy* **2021**, *79*, 105421.

[37] A. Alagumalai, M. Venu Rajendran, S. Ganesan, V. Sudhakaran Menon, R. K. Raman, S. M. Chelli, S. Muthukumar Vijayasayee, S. A. Gurusamy Thangavelu, A. Krishnamoorthy, *ACS Applied Energy Materials* **2022**, *5*, 6783.

[38] Y. Cai, J. Cui, M. Chen, M. Zhang, Y. Han, F. Qian, H. Zhao, S. Yang, Z. Yang, H. Bian, T. Wang, K. Guo, M. Cai, S. Dai, Z. Liu, S. (Frank) Liu, *Advanced Functional Materials* **2021**, *31*, 2005776.

[39] W. Zhao, J. Xu, K. He, Y. Cai, Y. Han, S. Yang, S. Zhan, D. Wang, Z. Liu, S. Liu, *Nano-Micro Letters* **2021**, *13*, DOI 10.1007/s40820-021-00688-2.

[40] Z. Wu, M. Jiang, Z. Liu, A. Jamshaid, L. K. Ono, Y. Qi, *Advanced Energy Materials* **2020**, *10*, 1903696.

[41] S. Fu, X. Li, L. Wan, Y. Wu, W. Zhang, Y. Wang, Q. Bao, J. Fang, *Advanced Energy Materials* **2019**, *9*, DOI 10.1002/aenm.201901852.

[42] K. Zou, Q. Li, J. Fan, H. Tang, L. Chen, S. Tao, T. Xu, W. Huang, *ACS Materials Letters* **2022**, *4*, 1101.

[43] D. Ma, J. He, J. Sheng, W. Shao, Z. Deng, R. Cen, Y. Fu, W. Wu, *J Mater Chem A Mater* **2024**, DOI 10.1039/d4ta05811a.

[44] J. Emara, T. Schnier, N. Pourdavoud, T. Riedl, K. Meerholz, S. Olthof, *Advanced Materials* **2015**, *28*, 553.

[45] B. Philippe, T. J. Jacobsson, J.-P. Correa-Baena, N. K. Jena, A. Banerjee, S. Chakraborty, U. B. Cappel, R. Ahuja, A. Hagfeldt, M. Odelius, H. Rensmo, *The Journal of Physical Chemistry C* **2017**, *121*, 26655.

[46] G. Wu, R. Liang, M. Ge, G. Sun, Y. Zhang, G. Xing, *Advanced Materials* **2022**, *34*, DOI 10.1002/adma.202105635.

[47] Z. Zhang, L. Qiao, K. Meng, R. Long, G. Chen, P. Gao, *Chemical Society Reviews* **2023**, *52*, 163.

[48] E. Shirzadi, F. Ansari, H. Jinno, S. Tian, O. Ouellette, Felix. T. Eickemeyer, B. Carlsen, A. Van Muyden, H. Kanda, N. Shibayama, F. F. Tirani, M. Grätzel, A. Hagfeldt, M. K. Nazeeruddin, P. J. Dyson, *ACS Energy Letters* **2023**, *8*, 3955.

[49] X. Liu, Z. Yu, T. Wang, K. L. Chiu, F. Lin, H. Gong, L. Ding, Y. Cheng, *Adv Energy Mater* **2020**, *10*, 2001958.

[50] J. M. Ball, A. Petrozza, *Nat Energy* **2016**, *1*, DOI 10.1038/nenergy.2016.149.

[51] Y. Zhang, Y. Zhu, M. Hu, N. Pai, T. Qin, Y.-B. Cheng, U. Bach, A. N. Simonov, J. Lu, *J Phys Chem Lett* **2022**, *13*, 2792.

[52] Y. Chen, W. Zhou, X. Chen, X. Zhang, H. Gao, N. A. N. Ouedraogo, Z. Zheng, C. B. Han, Y. Zhang, H. Yan, *Adv Funct Mater* **2021**, *32*, DOI 10.1002/adfm.202108417.

[53] Y. Huang, M. Tao, Y. Zhang, Z. Wang, Z. Sun, W. Zhang, Y. Xiong, X. Zong, Y. Wang, M. Liang, *Angewandte Chemie International Edition* **2024**, DOI 10.1002/anie.202416188.

[54] M. J. Jeong, S. W. Jeon, S. Y. Kim, J. H. Noh, *Adv Energy Mater* **2023**, *13*, DOI 10.1002/aenm.202300698.

[55] T. Li, Z. Zhang, F. He, L. Deng, Y. Yang, X. Mo, Y. Zhan, J. Liang, *Adv Funct Mater* **2023**, *33*, DOI 10.1002/adfm.202308457.

[56] Y. Chen, N. Li, L. Wang, L. Li, Z. Xu, H. Jiao, P. Liu, C. Zhu, H. Zai, M. Sun, W. Zou, S. Zhang, G. Xing, X. Liu, J. Wang, D. Li, B. Huang, Q. Chen, H. Zhou, *Nat Commun* **2019**, *10*, DOI 10.1038/s41467-019-09093-1.

[57] J. Kim, S.-H. Lee, J. H. Lee, K.-H. Hong, *J Phys Chem Lett* **2014**, *5*, 1312.

[58] Q. Wang, Y. Shao, Q. Dong, Z. Xiao, Y. Yuan, J. Huang, *Energy Environ. Sci.* **2014**, *7*, 2359.

[59] Y. Guo, J. Ma, H. Lei, F. Yao, B. Li, L. Xiong, G. Fang, *J Mater Chem A Mater* **2018**, *6*, 5919.

[60] G. Kim, G. Kang, K. Choi, H. Choi, T. Park, *Adv Energy Mater* **2018**, *8*, DOI 10.1002/aenm.201801386.

[61] Z. Li, M. Wu, L. Yang, K. Guo, Y. Duan, Y. Li, K. He, Y. Xing, Z. Zhang, H. Zhou, D. Xu, J. Wang, H. Zou, D. Li, Z. Liu, *Adv Funct Mater* **2023**, *33*, DOI 10.1002/adfm.202212606.

[62] X. Lian, J. Chen, S. Shan, G. Wu, H. Chen, *ACS Applied Materials & Interfaces* **2020**, *12*, 46340.

[63] Q. Xue, Y. Bai, M. Liu, R. Xia, Z. Hu, Z. Chen, X.-F. Jiang, F. Huang, S. Yang, Y. Matsuo, H.-L. Yip, Y. Cao, *Adv Energy Mater* **2016**, *7*, 1602333.

[64] M. Stolterfoht, C. M. Wolff, Y. Amir, A. Paulke, L. Perdigón-Toro, P. Caprioglio, D. Neher, *Energy Environ Sci* **2017**, *10*, 1530.

[65] J. Wang, J. Zhang, Y. Zhou, H. Liu, Q. Xue, X. Li, C.-C. Chueh, H.-L. Yip, Z. Zhu, A. K. Y. Jen, *Nat Commun* **2020**, *11*, DOI 10.1038/s41467-019-13909-5.

[66] Y. Xu, X. Guo, Z. Lin, Q. Wang, J. Su, J. Zhang, Y. Hao, K. Yang, J. Chang, *Angewandte Chemie* **2023**, *135*, DOI 10.1002/ange.202306229.

[67] S. Park, S. Y. Jeong, J. Kim, H. Lee, H. S. Kim, Y. W. Noh, Y. I. Kim, S. Cho, J. S. Kang, H. Y. Woo, M. H. Song, *Energy & Environmental Science* **2024**, *17*, 8304.

[68] V. Babu, R. Fuentes Pineda, T. Ahmad, A. O. Alvarez, L. A. Castriotta, A. Di Carlo, F. Fabregat-Santiago, K. Wojciechowski, *ACS Appl Energy Mater* **2020**, *3*, 5126.

[69] Y. Wang, W. Li, Y. Yin, M. Wang, W. Cai, Y. Shi, J. Guo, W. Shang, C. Zhang, Q. Dong, H. Ma, J. Liu, W. Tian, S. Jin, J. Bian, Y. Shi, *Adv Funct Mater* **2022**, *32*, DOI 10.1002/adfm.202204831.

[70] I. Zarazua, G. Han, P. P. Boix, S. Mhaisalkar, F. Fabregat-Santiago, I. Mora-Seró, J. Bisquert, G. Garcia-Belmonte, *J Phys Chem Lett* **2016**, *7*, 5105.

[71] D. Walter, Y. Wu, T. Duong, J. Peng, L. Jiang, K. C. Fong, K. Weber, *Adv Energy Mater* **2017**, *8*, DOI 10.1002/aenm.201701522.

[72] P. Chen, Q. Zheng, Z. Jin, Y. Wang, S. Wang, W. Sun, W. Pan, J. Wu, *Adv Funct Mater* **2024**, DOI 10.1002/adfm.202409497.

[73] T. Niu, J. Lu, R. Munir, J. Li, D. Barrit, X. Zhang, H. Hu, Z. Yang, A. Amassian, K. Zhao, S. (Frank) Liu, *Advanced Materials* **2018**, *30*, 1706576.

[74] N. Liu, J. Xiong, Z. He, C. Yuan, J. Dai, Y. Zhang, C. Zhou, X. Zhang, L. Li, D. Wang, Z. Zhang, Y. Huang, Q. Dai, J. Zhang, *Adv Energy Mater* **2023**, *13*, DOI 10.1002/aenm.202300025.

[75] Y. Yang, D. P. Ostrowski, R. M. France, K. Zhu, J. van de Lagemaat, J. M. Luther, M. C. Beard, *Nat Photonics* **2015**, *10*, 53.

[76] F. Liu, Q. Dong, M. K. Wong, A. B. Djurišić, A. Ng, Z. Ren, Q. Shen, C. Surya, W. K. Chan, J. Wang, A. M. C. Ng, C. Liao, H. Li, K. Shih, C. Wei, H. Su, J. Dai, *Advanced Energy Materials* **2016**, *6*, DOI 10.1002/aenm.201502206.

[77] F. Liu, Q. Dong, M. K. Wong, A. B. Djurišić, A. Ng, Z. Ren, Q. Shen, C. Surya, W. K. Chan, J. Wang, A. M. C. Ng, C. Liao, H. Li, K. Shih, C. Wei, H. Su, J. Dai, *Adv Energy Mater* **2016**, *6*, 1502206.

[78] S. Chen, X. Zhang, J. Zhao, Y. Zhang, G. Kong, Q. Li, N. Li, Y. Yu, N. Xu, J. Zhang, K. Liu, Q. Zhao, J. Cao, J. Feng, X. Li, J. Qi, D. Yu, J. Li, P. Gao, *Nat Commun* **2018**, *9*, DOI 10.1038/s41467-018-07177-y.

[79] A. Y. Grishko, A. A. Eliseev, E. A. Goodilin, A. B. Tarasov, *Chemistry of Materials* **2020**, *32*, 9140.

[80] Y. W. Seok, P. Byung-Wook, J. E. Hyuk, J. N. Joong, K. Y. Chan, L. D. Uk, S. S. Sik, S. Jangwon, K. E. Kyu, N. J. Hong, S. S. Il, *Science (1979)* **2017**, *356*, 1376.

[81] S. Yang, J. Dai, Z. Yu, Y. Shao, Y. Zhou, X. Xiao, X. C. Zeng, J. Huang, *J Am Chem Soc* **2019**, *141*, 5781.

[82] S. Chen, X. Xiao, H. Gu, J. Huang, *Sci Adv* **2021**, *7*, 1.

WILEY-VCH